RSC Advances

ROYAL SOCIETY OF CHEMISTRY

www.rsc.org/advances

Cite this: DOI: 10.1039/c0xx00000x

www.rsc.org/xxxxxx

ARTICLE TYPE

Template GNL-assisted Synthesis of Porous $Li_{1.2}Mn_{0.534}Ni_{0.133}Co_{0.133}O_2$: Towards High Performance Cathodes for Lithium Ion Batteries

Yanling Huang,[a] Xianhua Hou,[a, b]* Shaomeng Ma,[a] Xiaoli Zou,[a] Yuping Wu,[c] Shejun Hu,[a,b] Zongping Shao,[a,d] Xiang Liu[a,c]*

Received (in XXX, XXX) Xth XXXXXXXXX 20XX, Accepted Xth XXXXXXXXX 20XX
DOI: 10.1039/b000000x

Modified porous spherical $Li_{1.2}Mn_{0.534}Ni_{0.133}Co_{0.133}O_2$ has been successfully synthesized via a co-precipitation method, adopting graphene and carbon nanotube conductive liquid (GNL) as a template and surface modified material. The unique porous structure and the larger specific surface area of the porous $Li_{1.2}Mn_{0.534}Ni_{0.133}Co_{0.133}O_2$ contribute to both the increase in the first coulombic efficiency, from 76.3% to 82.0%, and the enhancement of the rate capability, demonstrating initial discharge capacities of 276.2, 245.8, 218.8, 203.9, 178.8, 135.9 and 97.5 mAh g^{-1} at different discharge rates of 0.1, 0.2, 0.5, 1.0, 2.0, 5.0 and 10 C, respectively. Even after suffering 100 cycles of charge-discharge, the porous Li-rich cathode can still deliver a discharge capacity of 235.5 mAh g^{-1}, suggesting a high capacity retention of 86.2% compared to the initial discharge capacity (273.3 mAh g^{-1}). Besides, the diffusion coefficient of the Li^+ investigated by cyclic voltammetry technique is approximately 10^{-12} cm^2 s^{-1}, indicating a faster kinetics of the lithium ions for the modified porous $Li_{1.2}Mn_{0.534}Ni_{0.133}Co_{0.133}O_2$ compared with the ordinary $Li_{1.2}Mn_{0.534}Ni_{0.133}Co_{0.133}O_2$ (~ 10^{-13} cm^2 s^{-1}). In fact, the introduction of GNL as a template not only leads to the porous structure of the Li-rich cathode material but also brings improvement to the crystallinity and size of the grains, which can be ascribed to the combined effect of the GNL with the carbonate precursors of MCO_3 (M = Mn, Ni, Co) during the recrystallization process.

***Keywords*:** Lithium ion batteries, Cathode material, $Li_{1.2}Mn_{0.534}Ni_{0.133}Co_{0.133}O_2$, Porous structure, Diffusion coefficient

1.Introduction

To date, lithium-ion batteries (LIBs) are playing a major role in electric vehicles (EVs) and hybrid electric vehicles (HEVs) by virtue of their high energy density, long cycling lifetime and environmental benignity et al. [1-3]. Consequently, it is of great significance to exploit LIBs as a sort of efficiently storing energy device to meet the stringent demand of high-power and high-capacity transportation applications [4]. However, further energy density enhancement of LIBs is mainly thwarted by the cathode capacity and its operating voltages [5], which urges the development and utilization of a novel composite cathode with well recognized properties. Thus, accelerated efforts are being directed toward developing cheaper, safer, faster charging capability, higher energy and higher voltage cathode materials for advanced LIBs.

Bearing this in mind, several alternative cathodes such as $LiNi_{1/3}Co_{1/3}Mn_{1/3}O_2$ [6], $LiNi_{0.5}Mn_{1.5}O_4$ [7], spinel $LiMn_2O_4$ [8] and olivine $LiFePO_4$ [9] have been intensely studied by many research groups. However, their specific capacity and energy density (120-200 mAh g^{-1}, 500-650 Wh kg^{-1}) [4, 10-13] are not satisfactory for the urgent need of high performance Li-ion batteries. It is worth noting that a novel class of lithium-rich layered cathode materials formulated as $xLi_2MnO_3 \cdot (1-x)LiMO_2$ (M = Mn, Co, Ni, etc.) reveal remarkable electrochemical properties (>250 mAh g^{-1}, about 1000 Whk g^{-1}) [11,14,15], which indicates the highly promising utilization in cathode materials of the Li-rich layered materials.

Li-rich oxide materials with layered-layered structures for LIBs have been the focus of great interest ever since they were synthesized by Thackeray et al. in 1991 [16,17] because of their large rechargeable capacities and high operating voltages. Li-rich cathode materials with the notation of $xLi_2MnO_3 \cdot (1-x)LiMO_2$ (M= Mn, Ni, Co, etc.) contain the rhombohedral $LiMO_2$ (M= Mn, Ni, Co, etc.) structure and monoclinic Li_2MnO_3 structure, both of which can be considered as layered α-$NaFeO_2$-type rock salt structures [11,12,18]. As a result, Li-rich layered oxides can offer more efficient ion transport owing to a two-dimension pathway for Li ions given by the layered-layered structure. In spite of these attractive merits, the substantial restrictions of lithium-rich oxides for their practical implementation in commercial lithium-ion batteries are their low initial coulombic efficiency, unsatisfactory rate performance and poor cyclic durability

[19,4,14].

Plenty of methods have been employed to synthesize and modify the Li-rich cathodes, and several effective methods such as morphological controlling [15], surface modification [20-26] and ion doping [27-29], have been enormously developed to resolve the aforementioned shortcomings. As for the mostly adoptive method of surface modification, researchers are now seeking for novel coating materials instead of the traditional coating materials like oxides [21,22], phosphates [25,26] and fluorides [23,24]. For instance, Jie Zhang et al. [4] obtained the modified $Li_{1.2}Ni_{0.13}Mn_{0.54}Co_{0.13}O_2$ using polyimide nanocoating, showing an initial discharge capacity of 274.1 mAh g^{-1} at 0.1C between 2.0 V and 4.8 V. However, the long term cyclability and the high rate capability of the coated material were not further explored in detail; Cong Liu et al. [7] adopted spinel component to stabilize high capacity layered electrodes, delivering enhanced properties of high coulombic efficiency of up to 90%. But the modified material delivers a capacity of only 240 mAh g^{-1} between 2.0 and 4.8 V at a current rate of 0.1 C. And Yufang Chen et al. [14] applied $LiNi_{0.5}Mn_{1.5}O_4$ as a spinel coating material to stabilize the Li-rich layered electrodes, which delivered enhancing properties of high initial discharge capacity of 298.6 mAh g^{-1}. In spite of the high capacity of the improved Li-rich layered material, the cycling performance under 0.1C was not satisfactory at all. Bohang Song et al. [30,31] promoted the electrochemical performance of the Li-rich layered cathode $Li(Li_{0.2}Mn_{0.54}Ni_{0.13}Co_{0.13})O_2$ using surface treatment with SP or graphene oxide, leading to increase in both the first coulombic efficiency and the rate capability. However, only limited reports can synthetically optimize the initial coulombic efficiency, the structural stability and the rate capability of the Li-rich cathode materials. Unlike the approaches mentioned above, we have concentrated on the facile synthesis of a kind of morphology controllable Li-rich cathode materials by using a novel template. And the electrochemical performance of the modified material is constitutionally elevated.

Since high temperature calcination in an oxygen atmosphere is involved in the fabrication of the Li-rich layered oxides, CNTs and graphene are rarely adopted in the calcination process due to drastic loss of carbon during the reaction with oxygen [31]. Herein, we have designed a strategy by employing GNL (Graphene and carbon nanotube conductive liquid, BTR Nano Tech Co.,Ltd.) as a template and surface modified material to synthesize a kind of porous structure Li-rich cathode material, aiming to enhance its initial coulombic efficiency, rate capability and specific capacity. The introduction of GNL in the design of a porous Li-rich cathode material $Li_{1.2}Mn_{0.534}Ni_{0.133}Co_{0.133}O_2$ shows expected results of outstanding high specific capacity (276.2 mAh g^{-1} at 0.1 C), excellent cycling stability (235.5 mAh g^{-1} after 100 cycles), and good rate capability (97.5 mAh g^{-1} at 10 C). This strategy might contribute to improve the morphology and especially the electrochemical performance of the Li-rich cathode materials and can be extended to other material synthesis for lithium-ion batteries.

2. Experimental

2.1. Synthesis of the porous spherical Li-rich materials Li1.2Mn0.534Ni0.133Co0.133O2

All chemicals (Sigma Aldrich), except for the GNL template, were of commercially available analytical grade and were used without further purification. The Li-rich cathode material $Li_{1.2}Mn_{0.534}Ni_{0.133}Co_{0.133}O_2$ was prepared by high-temperature calcinations of the spherical co-precipitation precursors of transition metals carbonate. Typically, 120 mL of Na_2CO_3 with a concentration of 1.0 M and 100mL of an aqueous solution containing metal acetates with a molar ratio Mn: Ni: Co of 0.534: 0.133: 0.133 (1.0 M) were added simultaneously into a continuously stirred mixed solution of 300 mL NH_4HCO_3 solution (0.5 M). The pH was adjusted to 7.5 - 8.0 using NH_4OH. After stirring for 4 h with a stirring speed of 800 rpm, the obtained precipitation was filtrated, rinsed with distilled water, and finally dried at 60 ℃ in an oven for 8 h. Then the precursor was mixed with stoichiometric amount of Li_2CO_3 (5% excess Li_2CO_3) by grinding, and subsequently preheated at 500 ℃ for 5 h and then calcined at 900 ℃ for 12 h in air atmosphere. The final product was named as ordinary LMNCO.

To prepare the porous Li-rich cathode material of $Li_{1.2}Mn_{0.534}Ni_{0.133}Co_{0.133}O_2$, the synthesis mechanism is shown in Scheme 1. Herein, the SEM image of the GNL (graphene and carbon nanotube conductive liquid, 5.7 % solid content, BTR Nano Tech Co., Ltd.) template is shown in the top left corner of **Scheme.1.** As is emerged, a great amount of CNTs are well-dispersed on the graphene sheets, and indeed, there are more CNTs dispersed in the conductive liquid than on the graphene sheets. Specifically, 1.5 g GNL was adopted and dispersed in 100 mL deionized water using ultrasonic in advance. Afterwards, the GNL suspension liquid was added into the above mentioned solution of NH_4HCO_3 (0.5 M). Identically, the following steps were all the same as the above mentioned processes and the final product was named as porous GNL-LMNCO.

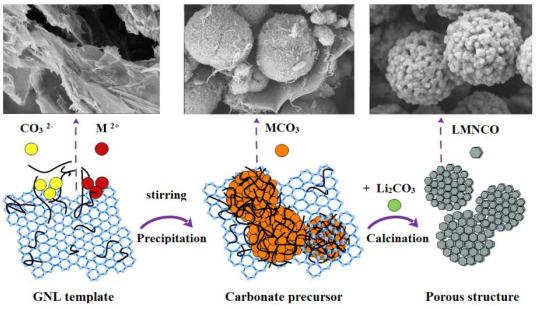

Scheme.1 The formation mechanism of the porous GNL-LMNCO.

2.2. Material characterization and electrochemical testing

The crystal structure, morphology, and the microstructural morphology of the as-prepared products were characterized by powder X-ray diffractometry (XRD; PANalytical X'pert PRO, Cu/K_α radiation, λ=0.15406 nm), scanning electron microscope (SEM, ZEISS ULTRA 55) and transmission electron microscopy (TEM; JEM-2100HR). The element contents were examined by energy-dispersive X-ray spectroscopy (EDS). The porous nature of the samples was investigated using physical adsorption of nitrogen at liquid-nitrogen temperature on an automatic volumetric sorption analyzer (NO-VA3200e, Quantachrome). The

specific surface area was determined according to the BrunauereEmmetteTeller (BET) method in the relative pressure range of 0.05-0.2. Pore size distribution (PSD) curves were derived from the BarretteJoynereHalenda (BJH) method using the adsorption branches.

The electrochemical performance was measured using coin-type half-cells (CR2430) assembled in an argon-filled glove box. The working electrode was made by mixing 80 wt.% LMNCO composite, 10 wt.% Super P as the conducting agent, and 10 wt.% PVDF as the binder. The electrode slurry was dispersed and spread onto aluminum foil (10 μm). After drying under vacuum at 80 ℃ for 12h, the electrodes were pressed and punched (φ=18 mm). The average loading mass of the electrodes was approximately 6.32 mg. The electrolyte was 1 M $LiPF_6$ in a mixture of EC/DEC/EMC (1:1:1 by volume, provided by Chei Industries Inc., South Korea). Metallic lithium foil (Aldrich) was employed as the counter and reference electrode, Celgard-2400 as the separator.

The charge-discharge performance of the cells were conducted between 2.0 and 4.65 V at a constant current densities of 25 - 2500 mA g^{-1} (1C = 250 mA g^{-1}) at 25 ℃ (CT2001A, LAND). Cyclic voltammetry (CV) measurements were carried out using a Solartron Analytical 1470E electrochemistry system at different scan rates of 0.1, 0.2, 0.4 and 0.8 mV s^{-1} between 2.5 V and 4.65 V. In this report, the lithiation was expressed as discharging, whereas the de-lithiation as charging.

3. Results and discussion

The XRD patterns of the ordinary LMNCO and porous GNL-LMNCO are illustrated in **Fig. 1**. With the exclusion of the low intensity reflections, in particular those between 20° and 25°, the major diffraction peaks in the XRD patterns can be indexed on the basis of a layered hexagonal α-$NaFeO_2$ structure with space group *R*-3*m* [11]. Besides, the weak reflections around 21° (marked with dashed line circles in Fig.1) correspond to the integrated monoclinic Li_2MnO_3 character (space group *C*2/*m*) **[35]**, originating from the super lattice ordering of the Li, Mn, Ni, and Co in the 3a site. No obvious diffraction peak assignable to any impurity phase is detected from the XRD patterns, indicating the successful formation of highly purified oxides. The complete splits of the (006)/(102) and (108)/(110) pairs reflections observed in all the XRD patterns are the signatures for a well-defined layered structure [11,33,34]. There is no much difference of the diffraction peaks in the XRD patterns between the porous GNL-LNMCO and the ordinary LMNCO, indicating that the original phase of the porous GNL-LNMCO had not changed by introducing of the GNL template in the synthesis process.

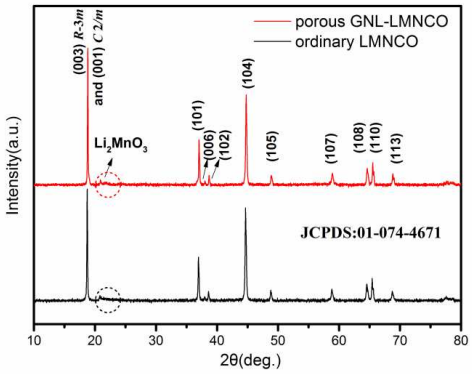

Fig. 1 XRD patterns of the ordinary LMNCO and the porous GNL-LMNCO.

The SEM images of the precursor of the ordinary LMNCO are shown in **Fig. 2a**. Detailed observation is made on a damaged sphere. The micron-sized sphere of the precursor is composed of thickly-dotted primary particles, which own the general size of approximately 35 nm. Besides, the precursor presents uniform and shapely spherical morphology, most of which own the size of 1.5 - 2.0 μm, as is delivered in the insert of **Fig. 2a**. What's more, uniform and shapely spherical carbonate precursors of the porous GNL-LMNCO can also be observed clearly in the SEM image of **Fig. 2b**. As is expected, the carbon nanotubes intertwine around the primary particles commendably, forming into secondary spheres with the size of approximately 2.0 μ m afterwards. Remarkably, the flake object emerged in **Fig. 2b** and **Fig. 4a** below can be referred to the graphene component of the GNL.

To better analyze the morphologies of the final products of the ordinary LMNCO and the porous GNL-LMNCO, some signs are marked in the SEM images of **Fig.2c** and **Fig. 2d** to distinguish the primary particles (marked with red squares) and the secondary particles (marked with red circles). The final products were obtained after calcination at a high temperature of 900℃. Dynamic recovery and recrystallization of the composite generate with the increasing of temperature. As is demonstrated in **Fig.2c** and its inset, the secondary particles of the ordinary LMNCO are composed of the primary particles, demonstrating a spherical morphology. Nevertheless, the grains are of uneven size. Some of the primary particles grow to large size of 1.0 μm and

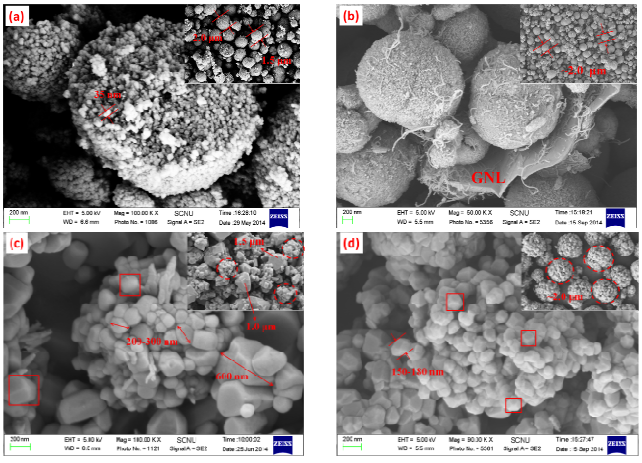

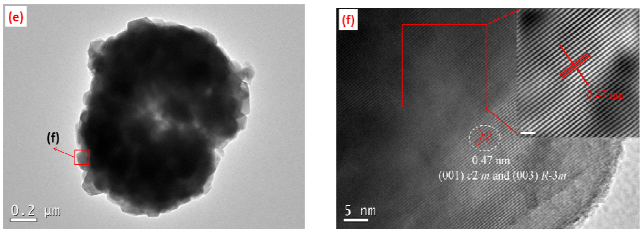

Fig. 2 Typical SEM images of (a) the precursors of the ordinary LMNCO; (b) the precursors of the porous GNL-LMNCO; (c) the ordinary LMNCO; (d) the porous GNL-LMNCO. (e) Representative TEM image of the porous GNL-LMNCO; (f) HRTEM image with illustrated crystal structure of the porous GNL-LMNCO.

even as large as 1.5 μm, much larger than the sizes of the smaller ones (200 - 300 nm), as is labeled in **Fig.2c**.

On the other hand, the GNL-LMNCO particles were obtained with a porous spherical structure after sintering. Herein, the porous structure was obtained as the gas of CO_2 released from the reaction of CNTs with the oxygen in air, and leave lots of pores and canals in the original position of CNTs. Dramatically, all of the primary particles are of the alike sizes (150-180 nm), as is exposed in **Fig. 2d**. In addition, the sizes of the primary particles of the porous GNL-LMNCO are more uniform than those of the ordinary LMNCO. In this respect, nano scaled particles with uniform size are widely recognized to be beneficial of providing a short path for Li^+ diffusion and increasing the specific surface areas, both of which can facilitate the excellent electrochemical performance [35]. Astonishingly, the spheres of the secondary particles (marked with **red** circles in **Fig. 2d**) almost own the same size of 2.0 μm and a great number of pores can be obviously detected from the stacking of the primary particles. As a matter of fact, during the calcination process, the combined effect of the GNL with the precursors of MCO_3 (M = Mn, Ni, Co) can delay the dynamic recrystallization and refine the grains and second phase particles considerably, resulting in beautiful porous spherical morphology of the porous GNL-LMNCO. The distinct angular appearance of the crystals observed from the SEM images of **Fig. 2d** probably suggests a higher degree of crystallinity of the porous GNL-LMNCO compared to the ordinary LMNCO, which is believed to be advantageous to the electrochemical performance in lithium ion batteries.

In particular, further observation of the porous GNL-LMNCO is made by TEM. As is demonstrated in the TEM images of **Fig. 2e**, the TEM image of the porous GNL-LMNCO shows its morphology of spheres, which is consistent with the SEM image of **Fig. 2d**. The contrast observed inside the sphere confirms the porosity of the porous GNL-LMNCO, which consists with the analysis of the SEM image in **Fig. 2d**. To analyze a microstructure with an atomic scale, high resolution (HR) TEM was performed. HRTEM image of the porous GNL-LMNCO (marked with the red rectangle in **Fig. 2e**), as is shown in **Fig. 2f**, exposes that the sample has clear parallel lattice fringes. The calculated interplanar spacing between two lattice fringes of the sample is approximately 0.47 nm, which can be ascribed to (003) planes from the rhombohedral phase $LiMO_2$ and/or (001) planes from the monoclinic Li_2MnO_3-like component. The result of the HRTEM investigation is in accordance with that of the XRD patterns and is also consistent with the primary reports [36,37].

To further confirm the porosity of the porous GNL-LMNCO, nitrogen isothermal adsorption-desorption measurement was conducted. The nitrogen adsorption-desorption BET isotherms of the porous GNL-LMNCO is shown in **Fig. 3a**. Between P/Po of 0.4-1.0, a distinct hysteresis loop was obtained. According to international union of pure and applied chemistry classification, the nitrogen adsorption-desorption isotherm can be classified as type IV category, indicating the characteristic of mesoporous and macropores materials. As can be observed from the pore size distribution spectrum in **Fig. 3b**, the mesopores and macropores of the porous GNL-LMNCO were mainly located in the range of 5 - 90 nm, and peaked at 43 nm, suggesting the presence of mesopores and macropores.

For comparison, the ordinary LMNCO was also presented with nitrogen isothermal adsorption-desorption measurement, as is shown in **Fig. 3c**. The nitrogen adsorption-desorption isotherm shows a type-III category, indicating the nonporous nature of the material. And the pore size distribution curve in **Fig. 3d** presents a jagged data. Furthermore, BET specific surface area of the porous GNL-LMNCO is 16.96 $m^2 g^{-1}$ compared with only 6.83 $m^2 g^{-1}$ for the ordinary LMNCO. Obviously, the increased specific surface area of the porous GNL-LMNCO was a result of the nano-sized primary particles and the porous structure of the Li-rich cathode material. At this point, the larger specific surface area can enlarge the electrochemical reaction areas and allow better penetration of the electrolyte [38-41], which is believed to be in favor of the electrochemical behavior, especially the capacity and cyclability [42,43].

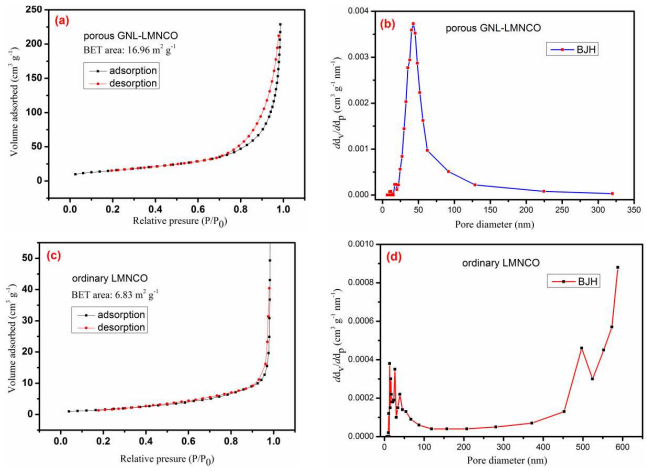

Fig. 3 Nitrogen adsorption-desorption BET isotherms and the pore-size distribution curve analyzed by Barrett-Joyner-Halenda (BJH) method of (a-b) the porous GNL-LMNCO and (c-d) the ordinary LMNCO.

The composition of the obtained porous GNL-LMNCO and its precursor were further confirmed by elemental analysis method. Firstly, the elemental distributions on the surface of the precursors of the GNL-LMNCO are monitored by EDS mapping, as is shown in **Fig. 4**. The qualitative uniform coverage of Mn, Ni, Co, C and O could be obtained and observed clearly from these figures. Different colors represent different elements, as is demonstrated in **Fig. 4**. Moreover, the quantitative analysis of the element distribution on the surface of the final product of GNL-LMNCO by EDS, with the profile shown in **Fig. 5a**, demonstrated that the element distribution of Mn, Ni, Co (**Fig. 5b**) is well-matched with the target ratio of the cathode material $Li_{1.2}Mn_{0.534}Ni_{0.133}Co_{0.133}O_2$. Specifically, Mn : Ni : Co = 9.62 : 2.39 : 2.40. There is an acceptable error in the identification results compared with the original ratio of Mn : Ni : Co = 0.534 : 0.133: 0.133.

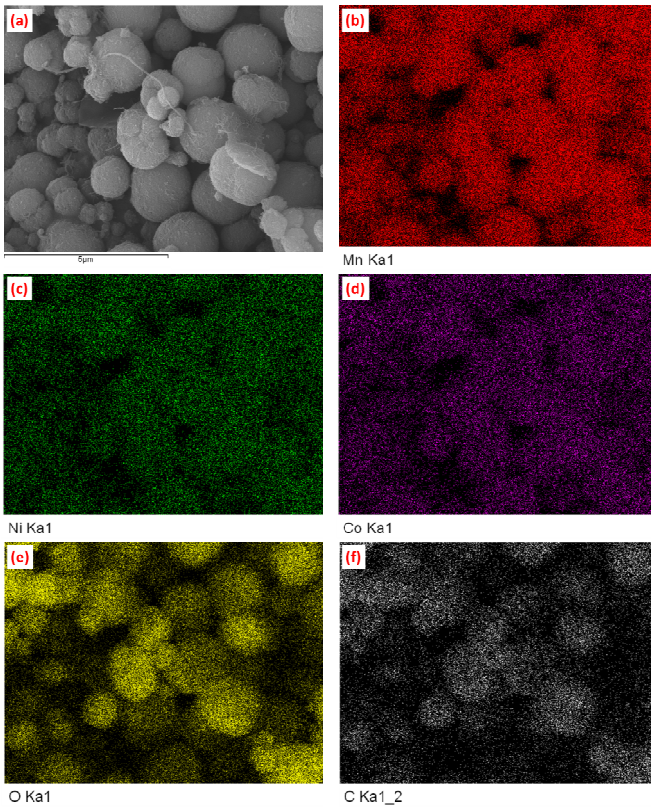

Fig. 4 SEM and EDS characterization of the precursor of the porous GNL-LMNCO: (a) HAADF SEM image and qualitative EDS mapping revealing the presence of (b) manganese (red),(c) nickel (green), (d) cobalt (magenta), (e) oxygen (yellow), and (f) carbon (gray).

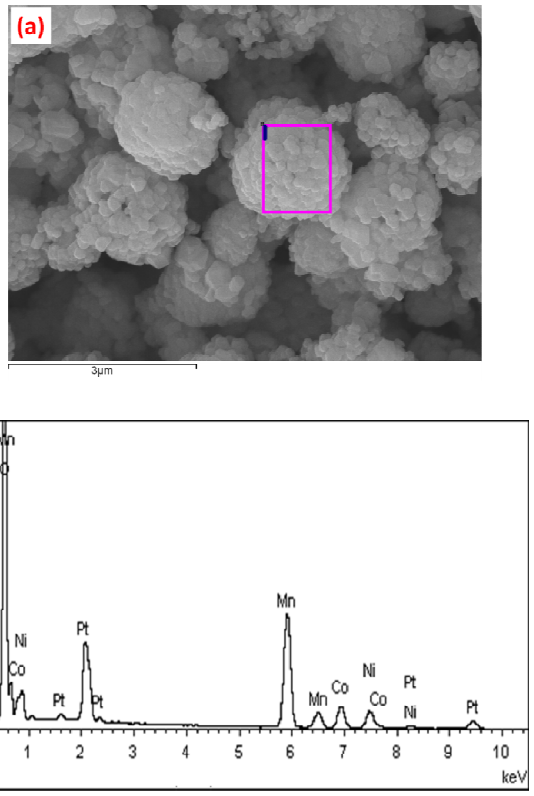

Fig. 5 (a) SEM image of the porous GNL-LMNCO; (b) EDS images of the selective area;

3.1. Electrochemical performance

Extended electrochemical tests such as constant current charge-discharge techniques were performed to study the structural effect on the two $Li_{1.20}Mn_{0.534}Ni_{0.133}Co_{0.133}O_2$ cathodes. The initial charge-discharge profile of the two cathode materials is presented in **Fig. 6a**. Located at 3.8 - 4.4 V and above 4.5 V, both of the materials exhibit two plateaus during the first charge, which are consistent with the normal Li-rich oxides. It is mainly ascribed to the existence of two different lithium ion extraction

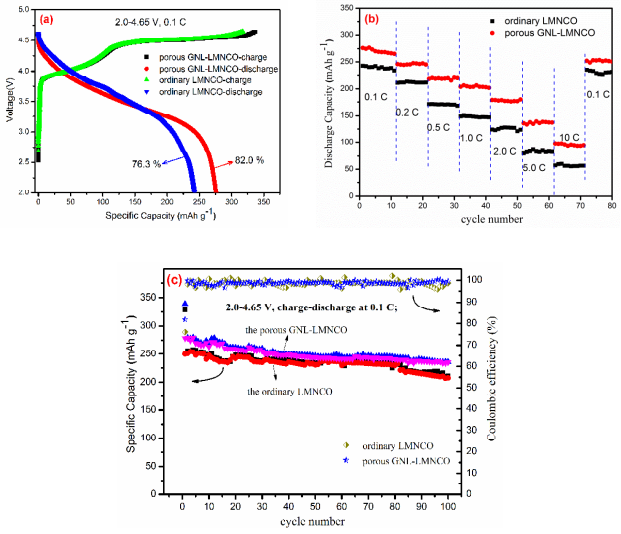

Fig. 6 Electrochemical performances of the porous GNL-LMNCO and the ordinary LMNCO electrodes as cycled in the voltage range between 2.0 V and 4.65 V at 25 ℃; (a) initial charge and discharge profiles at 0.1C; (b) rate performance at different rates of 0.1, 0.2, 0.5, 1.0, 2.0, 5.0 and 10 C, charged and discharged at the same rate; (c) cycling performance of 100 cycles at 0.1C.

processes [44]. The first plateau at 3.8 - 4.4 V is associated with the delithiation of the $Li_{1.20}Mn_{0.534}Ni_{0.133}Co_{0.133}O_2$-like regions that corresponds to the oxidation of $Ni^{2+}\rightarrow Ni^{4+}$ and $Co^{3+}\rightarrow Co^{4+}$. The second plateau located at above 4.5 V is widely considered to originate from simultaneously extraction of Li and O atoms (or Li_2O) from the layered Li_2MnO_3 lattice. The first discharge capacity of the porous GNL-LMNCO delivers 276.2 mAh g^{-1} in the voltage range of 2.0 - 4.65 V, with an initial coulombic efficiency of 82.0%. However, only 242.4 mAh g^{-1} of the discharge capacity is revealed for the ordinary LMNCO, and a lower initial coulombic efficiency of 76.3%. This improvement is mainly caused by the stability of the porous architecture structure and the larger specific surface area of the porous GNL-LMNCO, which promotes the surface Li storage capacities, and thus lead to a higher discharge capacity [45].

The cycling responses of 10 cycles for the samples at different C rates ranging from 2.0 V to 4.65 V were evaluated and shown in **Fig. 6b**. As can be seen from the discharge profiles of the initial cycle at various current rates shown in **Fig. 6b**, both of the two samples demonstrate gradual loss of discharge capacity accompanied with the current density increases. The decreased capacities at higher C-rates are mainly caused by the high polarization of the material at high currents. In this work, the porous GNL-LMNCO is capable of delivering a better capacity than the ordinary LMNCO, which is mainly ascribed to the smaller sizes and shorter Li^+ diffusion path of the porous GNL-LMNCO. Specifically, the porous GNL-LMNCO demonstrates initial discharge capacities of 276.2, 245.8, 218.8, 203.9, 178.8, 135.9 and 97.5 mAh g^{-1} at different discharge rates of 0.1, 0.2, 0.5, 1.0, 2.0, 5.0 and 10 C, respectively, as can be clearly observed from **Fig. 6b**, while the ordinary LMNCO expresses 242.4, 211.4, 170.9, 148.8, 123.9, 80.1 and 57.3 mAh g^{-1} at 0.1, 0.2, 0.5, 1.0, 2.0, 5.0 and 10 C, respectively. The capacity difference between the two samples is as high as 40.2 mAh g^{-1} when discharged at high current of 10 C (2500 mA g^{-1}), suggesting better rate capability of the porous GNL-LMNCO. It is noteworthy that when the current rate goes back to 0.1 C, the discharge capacity of the porous GNL-LMNCO material can return to 252.0 mAh g^{-1}, while the ordinary LMNCO returns to 234.0 mAh g^{-1}, indicating the more excellent reversibility of the capacity for the porous GNL-LMNCO material. The results of the rate performance are in concert with the study of the particle sizes in the SEM images of **Fig. 2c** and **Fig. 2d**.

Long term cycling stability along with the columbic efficiency of the porous GNL-LMNCO and the ordinary LMNCO in galvanostatic experiments are compared in **Fig. 6c**. It can be seen that the porous GNL-LMNCO shows better cycling performance than the ordinary LMNCO. As is observed in **Fig. 6c**, the porous GNL-LMNCO delivers an initial specific discharge capacity of 273.3 mAh g^{-1} at 25 mA g^{-1}. After being suffered 100 cycles, the discharge capacity can still maintain at 235.5 mAh g^{-1}, indicative of a high capacity retention of 86.2%. As for the ordinary LMNCO (**Fig. 6c**), only 207.8 mAh g^{-1} of the reversible capacity is measured after the 100th cycle. The cycling stability of initial capacity (249.9 mAh g^{-1}) after 100 cycles is 83.2% for the ordinary LMNCO, much lower than the porous GNL-LMNCO. The enhanced capacity and improved cycling performance of the porous GNL-LMNCO are significantly related to the combined properties of porous architecture and high specific surface area, in particular of the larger specific surface area, which facilitates the surface Li storage capacities and therefore increases the capacity and cyclability, corresponding to the BET analysis in **Fig. 3**.

Cyclic voltammetry (CV) measurements are performed to better understand the surface electrochemical behavior of the electrode and electrolyte during the charge-discharge process. CV curves of the first three cycles for the porous GNL-LMNCO and the ordinary LMNCO at a scan rate of 0.1 mV s^{-1} between 2.5 and 4.65 V are demonstrated in **Fig. 7a** and **7b**, respectively. There is a substantial difference between the first and the subsequent two cycles. Two pairs of oxidation peaks can be obviously discerned in the first cycle, one at 4.03 V and another at about 4.60 V, which is accordant with the initial charge-discharge curves in **Fig. 6a**. The first anodic peak located at 4.03 V corresponds to the oxidation of Ni^{2+} to Ni^{4+} and Co^{3+} to Co^{4+} [8]. Subsequently, the second anodic peak at about 4.60 V, which gradually disappears in the second and third cycles, is associated with the activation reaction of Li_2MnO_3 along with the removal of Li_2O from the Li_2MnO_3 regions [15, 33, 46]. In the following cathodic sweep, the strong reduction peaks at 3.82 V for the porous GNL-LMNCO and 3.73 V or 3.78 V for the ordinary LMNCO are attributed to the reduction of Ni^{2+} and Co^{3+}, while the minor ones detected at 3.30 V in Fig. 7a or 3.29 V in Fig. 7b are caused by the reduction of Mn^{4+}, which happen in the electrochemical reaction after the Li_2MnO_3 component has been electrochemically activated during the anodic sweep process [2]. Cathodic peaks in the three cycles of the porous GNL-LMNCO especially at 3.82 V are completely overlapped compared to the ordinary LMNCO, which indicates the improved cyclic reversibility of the electrochemical reactions. As is shown the CV curves, the porous GNL-LMNCO exhibits obviously shifted redox peaks to lower potentials (4.03 V to 3.85 V) than the counterpart in the ordinary

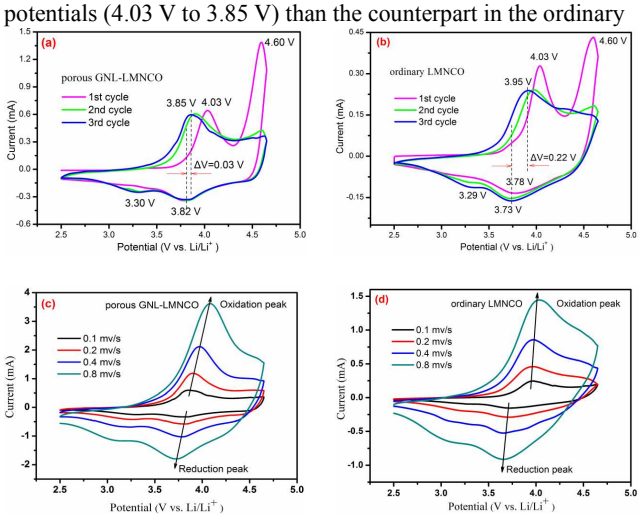

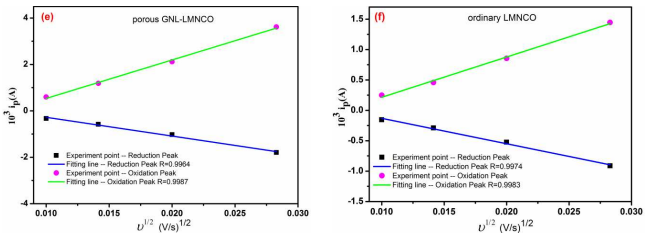

Fig. 7 Cyclic voltammograms measured in a potential range of 2.5-4.65 V (vs. Li/Li$^+$) at the scan rate of 0.1 mV s^{-1} for the first three cycles of (a) the porous GNL-LMNCO and (b) the ordinary LMNCO; Cyclic voltammograms measured at different scan rate of 0.1, 0.2, 0.4 and 0.8 mV s^{-1} for (c) the porous GNL-LMNCO and (d) the ordinary LMNCO; The current of peaks (i_p) vs the square root of scanning rates ($v^{1/2}$) plots of (e) the porous GNL-LMNCO and (f) the ordinary LMNCO.

LMNCO (4.03 V to 3.95 V) in the anodic sweep. It means that a smaller voltage difference of 0.03 V between the anodic peak and cathodic peak of the Ni ion and Co ion is obtained for the porous GNL-LMNCO, which can be understood by reduced polarization effect of the electrochemical processes [30] for the porous structure material.

CV analysis is also adopted to explore the reason for improved rate properties of the porous GNL-LMNCO compared with the ordinary LMNCO. **Fig. 7c** and **Fig. 7d** exhibit the CV curves of the porous GNL-LMNCO and ordinary LMNCO at different scan rates in the voltage range of 2.5 - 4.65 V. Both of the figures demonstrate that the peak height for the samples increases with the increase of the scan rate. Besides, the oxidation peaks shift to the positive direction while the reduction peaks shift to the negative direction with the increase of the scan rate. These phenomena probably owe to the higher polarization of the material at higher scan rate, which is recognized to have an important connection with the cycling behavior under high current densities. On the other side, **Fig. 7e** and **Fig. 7f** show cathodic and anodic peak currents (i_p) versus the square root of scanning rates plots for the electrodes. The lithium ion diffusion coefficient can be calculated according to the equation of *Randles-Sevcik* [47]:

$$i_p = (2.69\times10^5)n^{3/2} A\, D_{Li+}{}^{1/2}\, C\, \upsilon^{1/2}$$

where A is the effective area of electrode (2.54 cm^2), D_{Li+} is the lithium ion diffusion coefficient, n is the electron transfer numbers of oxidation-reduction reactions (here, n=1), υ is the scan rates, and C is the concentration of Li$^+$ (9.9748×10^{-2} mol cm^{-3}). As for the porous GNL-LMNCO, the lithium ion diffusion coefficient (D_{Li+}) of oxidation and reduction peaks calculated are 5.92×10^{-12} cm^2 s^{-1} and 1.41×10^{-12} cm^2 s^{-1}, respectively, while those of the ordinary LMNCO are 9.45×10^{-13} cm^2 s^{-1} and 3.77×10^{-13} cm^2 s^{-1} respectively, indicative of an enhanced kinetics of the lithium ions through the surface layer and the electrochemical reactions for the porous GNL-LMNCO. In fact, the improvement of kinetics during the Li insertion/extraction process is believed to be advantageous to the good rate capability of the electrode [48,49], which is intimately consistent with the results of the rate performance in **Fig. 6b**. What's more, as is shown in **Fig. 7e**, the fitting lines and the accuracy rating of the calculated diffusion coefficient of oxidation and reduction peaks for the porous GNL-LMNCO are 0.9964 and 0.9987, respectively, suggesting low errors of 0.36% and 0.13% and high reliability of the fitting data. Identically, the fitting data of the calculated diffusion coefficient for the ordinary LMNCO is of high reliability because of the high accuracy rating showed in **fig. 7f**. The pore canal caused by the carbon nanotubes provides a quick transfer channel for lithium ion, which is good for the electrode reaction during the transfer process of lithium ions and electrons, resulting in rapid electron transfer and hence a high rate capability.

To conclude, the outstanding cyclability and rate performance of the porous GNL-LMNCO can be attributed to several reasons given as follows. a) The porous structure enables to provide a buffer medium to accommodate the volume expansion of electrode materials during the electrochemical reaction process, ensuring the structure stability. b) The porous GNL-LMNCO owns larger specific surface area, which enlarges the electrochemical reaction areas and allows better penetration of electrolyte. In fact, this is beneficial for the fully charge and discharge reaction of Li$^+$ and thus elevates the specific capacity. c) The smaller and nano scaled particles is in favour of providing a short path for Li$^+$ diffusion and allowing the faster diffusion of Li$^+$, which can facilitate the excellent rate performance. Distinctively, CV investigation has been adopted to confirm the higher lithium ion diffusion coefficient and the improvement of kinetics during the Li insertion/extraction process of the porous GNL-LMNCO. Therefore, the porous GNL-LMNCO can perform a more superior property as a comparison with the ordinary LMNCO.

The performances of the porous GNL-LMNCO investigated above are preeminent compared with many other reported Li-rich cathodes [33,50-53].

4. Conclusions

In summary, modified porous spherical $Li_{1.2}Mn_{0.534}Ni_{0.133}Co_{0.133}O_2$ cathode material has been successfully synthesized by adopting GNL as a template and surface modified material via a co-precipitation method. The porous spherical structure of the $Li_{1.2}Mn_{0.534}Ni_{0.133}Co_{0.133}O_2$ was detected from both the SEM and TEM images, and was further investigated by nitrogen isothermal adsorption-desorption measurement. The larger initial coulombic efficiency of 82.0%, enhanced rate capability of 97.5 mAh g^{-1} at 10 C and increased specific capacity of 276.2 mAh g^{-1} at 0.1 C of the porous $Li_{1.2}Mn_{0.534}Ni_{0.133}Co_{0.133}O_2$ could be attributed to the smaller particle size and stable porous architecture structure compared with the nonporous ordinary $Li_{1.2}Mn_{0.534}Ni_{0.133}Co_{0.133}O_2$. Most importantly, the elevated Li$^+$ diffusion coefficient of 10^{-12} cm^2 s^{-1} for the porous GNL-LMNCO confirmed by CV technique suggests that the stable porous structure imparts a beneficial effect in terms of improving kinetics of the Li insertion/extraction process, and thus results in good rate capability. Essentially, this strategy might be a promising solution to improve the morphology, structural stability and therefore the electrochemical performance of the Li-rich cathode materials and can be extended to other material synthesis for lithium-ion batteries.

Acknowledgements

This work was financially supported by the National Science Foundation of China (NSFC, Nos. 51201066 and 51171065), the Natural Science Foundation of Guangdong Province (Nos. S2012020010937) and the Scientific Research Foundation of Graduate School of South China Normal University (Grant No. 2014ssxm16). The author also acknowledges ARC future fellowship.

Notes and references

[a] *Laboratory of Quantum Engineering and Quantum Materials, School of Physics and Telecommunication Engineering, South China Normal University, Guangzhou 510006, China*

[b] *Engineering Research Center of Materials & Technology for Electrochemical Energy Storage (Ministry of Education), Guangzhou 510006, China*

[c] *Institute of Advanced Materials, Nanjing University of Technology, Nanjing 210009, China*

[d] *Department of Chemical Engineering, Curtin University, Perth WA 6158, Australia*

*corresponding authors: Tel: +862039318011, *E-mail addresses: houxh@scnu.edu.cn (X. H. Hou); Liuxiang1962@126.com (X. Liu);*

References

1 A. R. Armstrong and P. G. Bruce, Nature, 1996, **381**, 499-500.
2 H. F. Li, J. Pang, Y. P. Yin, W. D. Zhuang, H. Wang, C. X. Zhai and S. G. Lu, RSC Adv., 2013, **3**, 13907-13914.
3 M. Li, X. H. Hou, Y. J. Sha, J. Wang, S. J. Hu, X. Liu and Z. P. Shao, J. Power Sources, 2014, **248**, 721-728.
4 J. Zhang, Q. W. Lu, J. H. Fang, J. L. Wang, J. Yang and Y. NuLi, ACS Appl. Mater. Interfaces, 2014, **6**, 17965-17973.
5 X. H. Hou, X. L. Zou, Y. L. Huang, S. J. Hu, Q. R and Y. M. Gao, RSC Adv., 2014, **4**, 29534-29541.
6 D. Mohanty, A. S. Mohanty, S. Kalnaus, J. L. Li, R. A. Meisner, E. A. Payzant, D. P. Abraham, D. L. Wood and C. Daniel, J Mater. Chem. A, 2013, **1**, 6249-6261.
7 C. Liu, Z. Y. Wang, C. S. Shi, E. Z. Liu, C. N. He and N. Q. Zhao, ACS Appl. Mater. Interfaces, 2014, **6**, 8363-8368.
8 H. Ming, Y. R. Yan, J. Ming, J. Adkins, X. W. Li, Q. Zhou and J. W. Zheng, Electrochim. Acta, 2014, **120**, 390-397.
9 Q. Wang, W. X. Zhang, Z. H. Yang, S. Y. Weng and Z. J. Jin, J. Power Sources, 2011, **196**, 10176-10182.
10 X. D. Xiang and W. S. Li, Electrochim. Acta, 2014, **133**, 422-427.
11 K. A. Jarvis, Z. Q. Deng, L. F. Allard, A. Manthiram and P. J. Ferreira, Chem. Mater., 2011, **23**, 3614-3621.
12 T. L. Zhao, S. Chen, R. J. Chen, L. Li, X. X. Zhang, M. Xie and F. Wu, ACS Appl. Mater. Interfaces, 2014, **6**, 21711-21720.
13 S. K. Martha, J. Nanda, Y. Kim, R. R. Unocic, S. Pannalab and N. J. Dudney, J. Mater. Chem. A, 2013, **1**, 5587-5595.
14 Y. F. Chen, K. Xie,C. M. Zheng, Z. Y. Ma and Z. X. Chen, ACS Appl. Mater. Interfaces, 2014, **6**, 16888-16894.
15 J. Q. Zhao and Y. Wang, J. Mater. Chem. A, 2014, **2**, 14947–14956.
16 C. S. Johnson, N. Li, J. T. Vaughey, S. A. Hackney and M. M. Thackeray, Electrochem. Commun., 2005, **7**, 528-536.
17 S. H. Park,; S. H. Kang, C. S.Johnson, K. Amine and M. M. Thackeray, Electrochem. Commun., 2007, **9**, 262-268.
18 F. Wu, N. Li, Y. F. Su, L. J. Zhang, L. Y. Bao, J. Wang, L. Chen, Y. Zheng, L. Q. Dai, J. Y. Peng and S. Chen, Nano Lett., 2014, **14**, 3550-3555.
19 H. J. Yu and H. S. Zhou, J. Phys. Chem. Lett., 2013, 4, 1268-1280.
20 F. Wu, Z. Wang, Y. Su, N. Yan, L. Bao and S. Chen, J. Power Sources, 2014, **247**,20-25.
21 X. Zhang, I. Belharouak, L. Li, Y. Lei, J. W. Elam, A. Nie, X. Chen, R. S. Yassar and R. L. Axelbaum, Adv. Energy Mater., 2013, **3**, 1299-1307.
22 J. Zhao, S. Aziz and Y. Wang, J. Power Sources, 2014, **247**,95-104.
23 J. M. Zheng, Z. R. Zhang, X. B. Wu, Z. X. Dong, Z. Zhu and Y. Yang, J. Electrochem. Soc., 2008, **155**, A775-A782.
24 Y. K. Sun, M. J. Lee, C. S. Yoon, J. Hassoun, K. Amine and B. Scrosati, Adv. Mater., 2012, **24**, 1192-1196.
25 J. R. Croy, M. Balasubramanian, D. Kim, S. H. Kang and M. M. Thackeray, Chem. Mater., 2011, **23**, 5415-5424.
26 D. Shin, C. Wolverton, J. R. Croy, M. Balasubramanian, S. H. Kang, C. M. L. Rivera and M. M. Thackeray, J. Electrochem. Soc., 2012, **159**, A121-A127.
27 Q. Li, G. S. Li, C. C. Fu, D. Luo,J. M. Fan and L. P. Li, ACS Appl. Mater. Interfaces, 2014, **6**, 10330-10341.
28 M. N. Ates, Q. Y. Jia, A. Shah, A. Busnaina, S. Mukerjee, K. M. Abraham, J. Electrochem. Soc., 2014, **161**, A290-A301.
29 W. He, D. Yuan, J. Qian, X. Ai, H. Yang, Y. Cao, J. Mater. Chem. A, 2013,**1**, 11397-11403.
30 B. H. Song, H. W. Liu, Z. W. Liu, P. F. Xiao, M. O. Lai and L. Lu., Scientific Reports, 2014, **3**, 3094-3106.
31 B. H. Song, M. O. Lai, Z. W. Liu, H. W. Liu and L. Lu, J. Mater. Chem. A., 2013, **1**, 9954-9965.
32 F. Li, S. X. Zhao, K. Z. Wang, B. H. Li and C. W. Nan, Electrochim. Acta, 2013, **97**, 17-22.
33 T. L. Zhao, S. Chen, L. Li, X.F. Zhang, R.J. Chen, I. Belharouak, F. Wu, K. Amine, J. Power Sources, 2013, **228**, 206-213.
34 X. Wei, S.C. Zhang, Z.J. Du, P.H. Yang, J. Wang, Y.B. Ren, Electrochim. Acta, 2013, **107**, 549-554.
35 Q. S. Xie, F. Li, H. Z. Guo, L. S. Wang, Y. Z. Chen, G. H. Yue and D. L. Peng, ACS Appl. Mater. Interfaces, 2013, **5**, 5508-5517.
36 Q. R. Xue, J. L. Li, G.F. Xu, H. W. Zhou, X. D. Wang and F. Y. Kang， J. Mater. Chem. A, 2014, **2**,18613-18623.
37 O. Toprakci, H. A. K. Toprakci, Y. Li, L. W. Ji, L. G. Xue, H. Lee, S. Zhang and X. W. Zhang, J. Power Sources, 2013, **241,** 522-528.
38 L. L. Hu, B. H. Qu, C. C. Li, Y. J. Chen, L. Mei, D. N. Lei, L. B. Chen, Q. H. Li and T. H. Wang, J. Mater. Chem. A, 2013, **1**, 5596-5602.
39 Y. G. Li, B. Tan and Y. Y. Wu, Nano Lett., 2008, **8**, 265-270.
40 G. H. Zhang, Y. J. Chen, B. H. Qu, L. L. Hu, L. Mei, D. N. Lei, Q. Li, L. B. Chen, Q. H. Li and T. H. Wang, Electrochim. Acta, 2012, **80**, 140-147.
41 J. H. Zhong, A. L. Wang, G. R. Li, J. W. Wang, Y. N. Ou and Y. X. Tong, J. Mater. Chem., 2012, **22**, 5656-5665.
42 J. F. Li, J. Z. Wang, X. Liang, Z. J. Zhang, H. K. Liu, Y. T. Qian and S. L. Xiong, ACS Appl. Mater. Interfaces, 2014, **6**, 24-30.
43 J. F. Li, J. Z. Wang, D. Wexler, D. Q. Shi, J. W. Liang, H. K. Liu, S. L. Xiong and Y. T. Qian, J. Mater. Chem. A, 2013, **1**, 15292-15299.
44 C. S. Johnson, N. Li, C Lefief and M. M. Thackerray, Electrochem. Commun., 2007, **9**, 787-795.
45 J. F. Li, S. L. Xiong, Y. R. Liu, Z. C. Ju and Y. T. Qian, ACS Appl. Mater. Interfaces, 2013, **5**, 981-988.
46 S. J. Shi, J. P. Tu, Y. Y. Tang, Y. X. Yu, Y. Q. Zhang and X. L. Wang, J. Power Sources, 2013, **221**, 300-307.
47 J. X. Wang, Z. X. Wang, X. H. Li, H. J. Guo, X. W. Wu, X. P. Zhang and W. Xiao, Electrochim. Acta, 2013, **87**, 224-229.
48 Y. S. Bai, X. Y. Wang, S. Y. Yang, X. Y. Zhang, X. K. Yang, H. B. Shu and Q. Wu, J. Alloys Comp., 2012, **541**, 125-131.
49 S. Y. Yang, G. Huang, S. J. Hu, X. H. Hou, Y. Y. Huang, M. Yue and G. T Lei, Mater. Lett., 2014, **118,** 8-11.
50 S. J. Shi, Z. R. Lou, T. F. Xia, X. L. Wang, C. D. Gu and J. P. Tu, J. Power Sources, 2014, **257**, 198-204.
51 P. Manikandan, P. Periasamya and R. Jagannathan, RSC Adv., 2014, **4**, 40359-40367.
52 X. W. Miao, Y. Yan, C. G. Wang, L. L. Cui, J. H. Fang and G. Yang, J. Power Sources, 2014, **247**, 219-227.
53 Z. Y. Zhu and L. W. Zhu, J. Power Sources, 2014, **256**, 178-182.

A table of contents entry

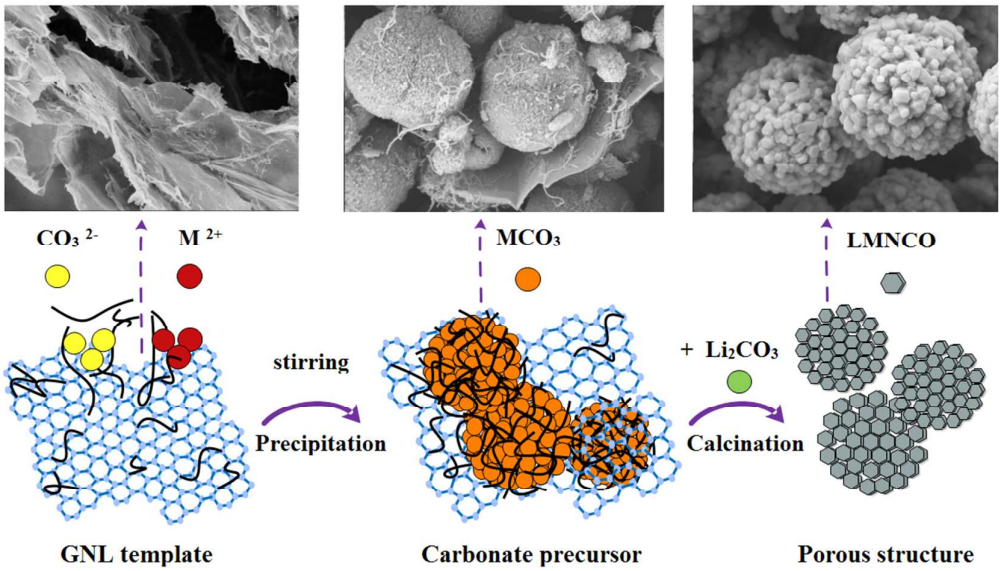

A High Performance Cathode of Porous $Li_{1.2}Mn_{0.534}Ni_{0.133}Co_{0.133}O_2$ for Lithium Ion Batteries Synthesized by a GNL-Template.